



Investigation of the γ' Precipitates Dissolution in a Ni-Based Superalloy During Stress-Free Short-Term Annealing at High Homologous Temperatures

ŁUKASZ RAKOCZY, MAŁGORZATA GRUDZIEN-RAKOCZY, FABIAN HANNING, GRZEGORZ CEMPURA, RAFAŁ CYGAN, JOEL ANDERSSON, and ANNA ZIELIŃSKA-LIPIEC

The equiaxed Ni-based superalloy René 108 was subjected to short-term annealing at five temperatures between 900 °C and 1100 °C. The phase composition, phase lattice parameters, microstructure, stereological parameters, and chemical composition of γ' precipitates were investigated by thermodynamic simulations, X-ray diffraction, scanning and transmission electron microscopy, and energy-dispersive X-ray spectroscopy. Analysis of the γ and γ' lattice parameters using the Nelson-Riley extrapolation function showed that the misfit parameter for temperatures 900 °C to 1050 °C is positive (decreasing from 0.32 to 0.11 pct). At 1100 °C, the parameter becomes negative, $\delta = -0.18$ pct. During the short-term annealing, γ' precipitates dissolution occurred progressing more rapidly with increasing temperatures. The surface fraction of γ' precipitates decreased with increasing temperature from 0.52 to 0.34. The dissolution of γ' precipitates did not only proceed through uninterrupted thinning of each individual precipitate, but also included more complex mechanisms, including splitting. Based on transmission electron microscopy, it was shown that after γ' precipitates dissolution, the matrix close to the γ/γ' interface is strongly enriched in Co and Cr and depleted in Al.

<https://doi.org/10.1007/s11661-021-06420-4>
© The Author(s) 2021

I. INTRODUCTION

NICKEL-BASED superalloys are characterized by very high mechanical properties, as well as resistance to corrosion and oxidation at high homologous temperatures, making them an important group of materials in the energy, nuclear, and aviation industries.^[1] The Ni-based superalloys are usually strengthened by the intermetallic γ' phase, which has an L1₂-type ordered structure. The γ' precipitates characteristics, including the size, volume fraction, distribution, and morphology,

directly determine their strength during long-term service.^[2–5] Several experiments have focused on the γ' precipitates' stability under short-term exposure at high homologous temperatures.^[6–11] Cormier *et al.*^[10] indicated that since the material can be subjected to short-time exposure at very high temperatures during in-service conditions, dissolution kinetics may also be an essential feature, i.e., long times at low temperatures may be less harmful than shorter times at very high temperatures. As stated, based on the MC2 superalloy investigations, a slight increase in temperature significantly affects the stability of the γ' precipitates, likely to cause a drastic decrease in mechanical properties due to the drop in structural hardening. Giraud *et al.*^[11] based on the study of the CMSX-4 superalloy stated that the dissolution kinetics depends on the initial γ' precipitates' morphology, coherency stress relaxation, as well as accumulated plastic strain. An increase in the accumulated plastic strain leads to an increase in the dissolution kinetics relative to the variant without the applied stress.

Preheating before welding is also considered as a short-term heat treatment cycle. Preheating is usually recommended by the welding community to limit thermal gradients (K/m) during cooling, thus improving the material's resistance to hot cracking.^[12] Preheating

ŁUKASZ RAKOCZY, GRZEGORZ CEMPURA, and ANNA ZIELIŃSKA-LIPIEC are with the AGH University of Science and Technology, Faculty of Metals Engineering and Industrial Computer Science, Mickiewicza 30, 30-059 Kraków, Poland Contact e-mail: lrakoczy@agh.edu.pl MAŁGORZATA GRUDZIEN-RAKOCZY is with the Łukasiewicz Research Network-Krakow Institute of Technology, Zakopiańska 73, 30-418 Kraków, Poland. FABIAN HANNING and JOEL ANDERSSON are with the University West, Department of Engineering Science, Gustava Melins Gata 2, 46132 Trollhättan, Sweden. RAFAŁ CYGAN is with the Consolidated Precision Products Corporation, Investment Casting Division, Hetmańska 120, 35-078 Rzeszów, Poland.

Manuscript submitted March 12, 2021; accepted July 29, 2021.

Article published online September 6, 2021

temperature and time, i.e., the influence of short-term heat treatment cycles on nickel superalloy's microstructure changes, is a particularly important area in designing new technologies, as welding processes are widely used for regenerating foundry defects and repairing of serviced components.^[13–16] Hot cracking, including liquation cracking in the heat-affected zone, is directly dependent on the γ' behavior during heating and subsequent cooling. Superalloys with more than 40–50 pct of γ' precipitates are commonly considered as difficult to weld.^[17–19] Various works have been reported for the welding repair of nickel-based superalloys with high γ' volume fractions (characterized by high susceptibility to cracking) with additional preheating.^[20–22] Danis *et al.*^[23] confirmed that the cracking of Inconel 738LC could be eliminated only by preheating. The temperature should be high enough to decrease the thermal gradient during welding, as much as possible; however, it should not induce significant changes in the initial microstructure. The beneficial effect of preheating on the decrease of susceptibility to hot cracking was also confirmed by Bidron *et al.*^[24] during experiments aimed to design a repair welding technology for the CM247LC superalloy. They presented that with induction preheating to 1050 °C, crack-free welds could be obtained in a multi-bead configuration. Based on scanning electron microscopy (SEM) observation, this was attributed to a reduction in γ' precipitates volume fraction. Simultaneously, they noted that further works are needed to explain the influence of the induction preheating stages on the microstructural changes, including γ' precipitates dissolution. The selection of preheating parameters should also take into account that after repairing with preheating, a full heat treatment (usually solutionizing + aging) should be applied to the repaired component to obtain the desired stable microstructure and high mechanical strength. High preheating temperatures can enable the dissolving of the high volume fraction of γ' precipitates, whereas exceedingly high temperatures and subsequent heat input originating from welding may lead to excessive degradation of the microstructure, including incipient melting of many eutectic γ/γ' islands.

The René 108 alloy used in this work is a conventionally cast polycrystalline Ni-based superalloy characterized by a high volume fraction (around 63 pct) of the γ' precipitates.^[25,26] The material in a fully heat-treated condition is characterized by a relatively complex microstructure. Dendrite cores and arms consist of secondary and tertiary γ' precipitates and (Cr, W)₅B₃ nanoborides with a size around 50 nm at the γ/γ' interfaces.^[27] In interdendritic regions, primary γ' precipitates, (Ta, Hf)C carbides with various morphologies and M₂₃C₆ nanocarbides, have additionally been detected. The M₂₃C₆ nanocarbides form during aging, according to the phase transformation reaction $MC + \gamma \rightarrow M_{23}C_6 + \gamma'$. A widely known MC carbide degradation reaction was observed in other works.^[28,29] This work aims to analyze the microstructural changes and to compare γ' precipitates' stability after short-term exposure to high temperatures. The obtained results will contribute to filling the existing knowledge gap about the René 108 and provide a better understanding on

microstructural evolution occurring during the initial stage of the γ' precipitates dissolution process in the René 108 superalloy. In particular, the short-term annealing is one of the methods of improving the weldability of the Ni-based superalloys with a high volume fraction of γ' precipitates. As the microstructure within the interdendritic regions is complex and far from the equilibrium state, special attention was given to the dendrite cores.^[27]

II. METHODOLOGY

A. Material

The René 108 nickel-based superalloy was used as the experimental alloy. Chemical composition as measured by means of optical emission spectroscopy (OES) is presented in Table I.

Lost-wax castings were subjected to heat treatment under vacuum with the following parameters: solutionizing at 1200 °C for 2h and aging at 900 °C for 8h. The casting was cooled very slow because the heat treatment was performed in the vacuum furnace. The cooling rate was 15 °C/min. down to 500 °C and then faster by argon blowing. The morphology of the γ' precipitates after heat treatment is presented in Figure 1. For the short-term annealing experiments the material (plates: 10×10×3 mm) was inductively heated (Dacpol Ambrell Ekoheat device) at a rate of 150 °C/min. to the set temperature, with a 3 minutes dwell time, and then cooled in ice water to obtain a microstructure as close as possible to that at high temperature (Figure 2). Two independent pyrometers were used for temperature control. The temperature precise was ± 5 °C. According to Semiatin *et al.*^[30] the cooling rate of the PM superalloy LSHR in water from 1190 °C is around 255.3 K/s (measured in 1 mm below the surface).

Microstructure observations and analyses were carried out using several techniques: thermodynamic simulations, X-ray diffraction (XRD), scanning electron microscopy (SEM), transmission electron microscopy (TEM), energy-dispersive X-ray spectroscopy (EDX), and high angle annular dark field scanning transmission electron microscopy (HAADF-STEM).

B. Thermodynamic Simulations

The thermodynamic simulations, using ThermoCalc software (version 2021a, Stockholm, Sweden) (database TCNI10:Ni-Alloys, ed. 2021a) were performed to calculate the maximum solubility of the selected alloying elements in the γ matrix at three temperatures: 900 °C, 1000 °C, and 1100 °C and phase stability in the temperature range 700 °C to 1400 °C.

C. XRD

XRD experiments were performed on a Bruker D8 Advance (Co K α radiation, $\lambda = 1.79$ Å) diffractometer in Bragg–Brentano geometry. Measurements were done in the range of $2\theta = 30$ to 130 deg with a step size of

Table I. Chemical Composition of the René 108 Nickel-Based Superalloy, Wt Pct

Element	Cr	W	Co	Al	Ta	Hf	Ti	Mo	C	B	Zr	V	Fe	Si	Ni	Others
Concentration	11.40	8.85	8.19	6.35	3.55	1.52	0.75	0.45	0.08	0.015	0.014	0.04	0.07	0.04	bal.	P-0.006, S-0.0002
Standard Deviation	0.08	0.04	0.04	0.08	0.09	0.06	0.008	0.006	0.001	0.0015	0.0004	0.002	0.0003	0.003		

0.04 deg on the polished specimens (face surface of the annealed plates). The angles of the peak positions were used to calculate the interplanar spacings d_{hkl} for each plane via using the Bragg-Wulff equation (Eq. [1]). Deconvolution for the double-peaks ($\gamma + \gamma'$) were fitted by well-known procedures using the least-square method to determine structure parameters. The matrix and γ' precipitate lattice parameters were calculated based on the XRD data using the Nelson-Riley^[31] extrapolation function (Eq. [2]). Based on the computed lattice parameter of the matrix a_γ and precipitates $a_{\gamma'}$, the misfit parameter δ was determined (Eq. [3]).

$$d_{hkl} = \frac{\lambda}{2 \sin \theta} \quad [1]$$

$$f(\theta) = \left(\frac{\cos^2 \theta}{\sin \theta} \right) + \left(\frac{\cos^2 \theta}{\theta} \right) \quad [2]$$

$$\delta = \frac{2(a_{\gamma'} - a_\gamma)}{a_{\gamma'} + a_\gamma} \quad [3]$$

D. SEM and TEM

Metallographic specimens were precision wet cut from the prepared annealed samples (to dimensions: 5×5×3 mm), ground with SiC sandpaper and then polished using diamond suspension (3, 1, and 0.25 μm). Quantitative analysis of the γ' precipitates was carried out using ImageJ software (National Institutes and the Laboratory for Optical and Computational Instrumentation, University of Wisconsin, Madison, WI). The surface fraction of γ' precipitates was estimated by the relative space taken up by a given microstructure constituent is the area fraction occupied by this constituent on the unit plane of the specimen. The size of γ' precipitates in dendrite cores was represented as the equivalent diameter (Eq. [4]). The measurements were conducted in several locations (more than 3000 precipitates) based on 10 images captured at area 180 μm^2 (magnification x20000). A SEM Phenom XL with 20 kV accelerating voltage was used. SEM backscattered electron images were binarized and subjected to a despeckle filter, which removed noise without blurring the edges. The area (A) and perimeter (P) of each γ' precipitate (assumed area range 0.03 to 5.0 μm^2) were measured. To evaluate γ' precipitate morphology changes, the circularity (Eq. [5]) was calculated.

$$\bar{\phi} = \sqrt{\frac{4A}{\pi}} \quad [4]$$

$$\zeta = \frac{4\pi A}{P^2} \quad [5]$$

where A area of γ' precipitate, μm^2 ; P perimeter of γ' precipitate, μm .

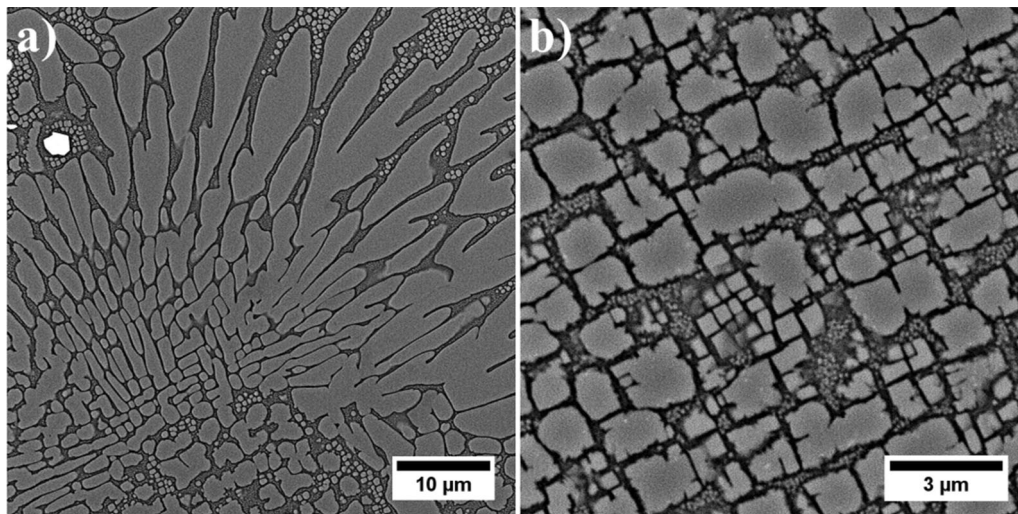


Fig. 1—Morphology of the γ' precipitates in the initial condition: (a) primary γ' in interdendritic region; (b) secondary and tertiary γ' in dendrite core. SEM-BSE contrast.

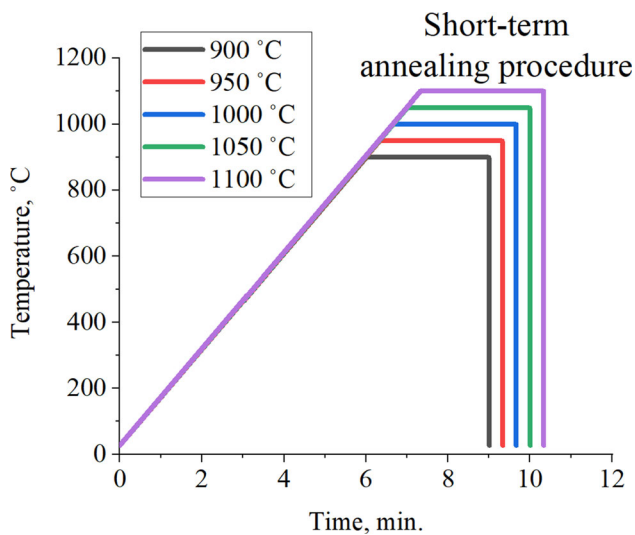


Fig. 2—Short-term annealing procedure.

The specimens subjected to short-term annealing at 1100 °C were investigated in more detail via TEM using bright field (BF), selected area electron diffraction (SAED) and HAADF-STEM methods. Samples were firstly ground down mechanically to about 0.05 mm thickness, after which 3 mm disks were punched and dimpled using a Gatan dimple grinder (Gatan, Inc., Pleasanton, CA) on both sides. The final step was thinning by Ar⁺ ion beam (PIPS of Gatan) at low angles. Before loading into the microscope, the thin foils were plasma cleaned (NanoMill 1040 Fischione) to remove surface contaminations. Initial microstructural observations were performed with a JEM-200CX (JEOL Ltd., Akishima, Japan) TEM. Higher magnification investigations, including atomic-scale resolution and chemical composition measurements (mapping), were

carried out with the Cs-corrected probe FEI Titan³ G2 60-300 TEM with ChemiSTEM system (Thermo Fisher Scientific, Eindhoven, Netherlands). The accelerating voltage was 200 kV. To reveal the position of diffraction peaks of selected precipitates, the HAADF-STEM images were subjected to Fast Fourier Transformation (FFT). The JEMS software (JEMS-SWISS, Jongny, Switzerland) was applied to fit the diffraction peaks.

III. RESULTS AND DISCUSSION

A. Solubility of Alloying Elements in γ Matrix and Phase Stability Calculated by ThermoCalc Software

During heating and holding at elevated temperature, it is expected that the strengthening precipitates (mainly γ') will start to dissolve in the matrix, enriching it with alloying elements. Table II shows the atomic radius calculated from minimal-basis-set wavefunctions^[32] and solubility data of various elements in γ matrix at 900 °C to 1100 °C, calculated by thermodynamic simulations with ThermoCalc. For comparison, the initial concentration of selected alloying elements in the René 108 superalloy, expressed at atomic percent, is also presented. The atomic radius of γ' -formers, i.e., Hf, Ta, and Ti, (2.08 Å, 2.00 Å, and 1.76 Å) is greater than that of nickel (1.49 Å), leading to an increase in the lattice parameter. Only aluminum has a smaller atomic radius (1.18 Å). W and Cr have the highest solubility in the matrix, 14.84 and 41.40 at. pct, respectively, at 900 °C. With the increase in temperature to 1100 °C, W and Cr's solubility in the γ matrix also increases. The γ' with the stoichiometric formula Ni_3Al is the main strengthening phase in the René 108 superalloy. The solubility of Al in Ni during heating from 900 °C to 1100 °C changes from 14.38 to 16.94 at. pct. The other alloying elements, i.e., Ti, Ta and Hf can substitute Al in the γ' unit cell. From these elements, Hf is characterized by the lowest

solubility in nickel, only 0.86 at. pct at 1100 °C. Additionally, carbon tends to form MC carbides with Hf, Ta, Ti, and W. Furthermore, the low solubility of B in Ni throughout all temperatures (not more than 0.41 at. pct at 1100 °C) is beneficial for the formation of borides.

Figure 3 shows the change in the amount of phases with increasing temperature. In the beginning, the structure mostly consists of two phases, γ and γ' ; however, the γ' precipitates clearly dominate. An increase in temperature leads to a gradual decrease in the amount of γ' precipitates. After exceeding the temperature of about 1052 °C, the γ phase begins to dominate although the γ' solvus temperature is 1281 °C. The amount of MC carbides and M_5B_3 boride precipitates in the set temperature range does not exceed 0.01 mol. Upon reaching approx. 1282 °C, only a slight decrease in the amount of carbides is observed. Only after exceeding this temperature, intensive carbides dissolution takes place. The M_5B_3 borides are very stable in the range of 700 °C to 1120 °C and their share in the microstructure almost does not change, while exceeding 1120 °C leads to rapid dissolution. The results obtained with ThermoCalc indicated that small amounts of liquid phase might appear after the dissolution of the M_5B_3 borides. Solutionizing is performed at 1200 °C, but any local melting did not observe after the heat treatment. In thermodynamic simulations, it is assumed that Cr occupies the M position. The STEM-EDX measurements showed that borides in the René 108 superalloy have significant amounts of W and Mo, which could increase their solvus temperature and consequently solidus temperature.^[27]

B. Influence of the Short-Term Annealing Temperature on the γ/γ' Misfit Coefficient

The misfit change with temperature was subjected to analysis as even small changes in the misfit can be attributed to significant γ' precipitates morphology evolution. The samples were subjected to XRD analysis in the range of $2\theta = 30$ to 130 deg (Figure 4(a)). On the XRD spectra, the presence of peaks from (111), (200), (220), (311), and (222) planes of the γ and γ' phases is confirmed. Additionally, peaks from the γ' phase, (210) and (221), MC carbides, (111) and (200) were identified.

The peaks at an angular position of about 53 and 79 deg are assigned to the M_5B_3 borides.^[33] The variable intensity of the peaks is characteristics of superalloys after the short-term exposure to high temperatures. This results mainly from the random crystallographic orientation of grains during casting. However, such texturing is typical for polycrystalline Ni-based superalloys produced by means of investment casting.^[34]

The double-peaks were separated to obtain peaks from the γ and γ' phases. It should be noted that the data correspond to all γ' precipitates present in the microstructure, namely primary, secondary, and the tertiary ones. The lattice parameters of the matrix and the precipitates were calculated based on the Nelson-Riley extrapolation function (Eq. [2]) (Figure 4b). With the increase in the annealing temperature, the γ' lattice parameter decreases from 3.60 Å (900 °C) to 3.58 Å (1100 °C). No such trend is observed for the matrix's lattice parameter. The a_γ values are in the range of 3.58 to 3.59 Å. The misfit parameter for 900 °C to 1050 °C preheat temperatures is positive. At 900 °C, the misfit is 0.32 pct, whereas at 950 to 1050 temperature range small fluctuations are visible, with δ changing from 0.16 pct through 0.19 to 0.11 pct. Only for 1100 °C a negative misfit value of $\delta = -0.18$ pct was attained.

C. Influence of the Annealing Temperature on the Dissolution of the γ' Precipitates

The SEM observations were performed to characterize the microstructure after the short-term annealing (Figure 5). The dendritic structure and irregular distribution of the microstructural constituents remains. Precipitates with a bright phase contrast (high Z-number) are MC carbides, and their surface fraction in each variant is less than 1 pct. They are characterized by inhomogeneous distribution in the casting volume, which corresponds to differences in the local surface fraction. Precise calculation of their volume fraction change with annealing temperature exposure could not be realized. More detailed observations allowed to conclude that the carbides are characterized by a very high thermodynamical stability, as predicted by the ThermoCalc simulation and if any dissolution occurred it was limited to only local regions (Figure 6). Far-reaching changes occurred in the case of intermetallic γ'

Table II. Solubility of the Selected Alloying Elements in γ Phase at 900 °C, 1000 °C, and 1100 °C

Element	Radius, Å ^[32]	Initial Concentration in René 108, At. Pct	Solubility in γ Phase, Wt Pct/At. Pct		
			900 °C	1000 °C	1100 °C
Al	1.18	13.94	7.17/14.38	7.83/15.60	8.57/16.94
Ta	2.00	1.17	12.87/4.57	14.59/5.25	17.08/6.27
Hf	2.08	0.49	0.78/0.26	1.51/0.50	2.58/0.86
Ti	1.76	0.98	8.58/10.32	9.67/11.60	10.79/12.92
W	1.93	2.85	35.51/14.84	37.38/16.01	38.27/16.52
Cr	1.66	12.89	38.49/41.40	42.01/44.99	44.85/47.86
B	0.87	0.11	0.019/0.10	0.041/0.22	0.075/0.41
C	0.67	0.39	0.162/0.79	0.235/1.14	0.323/1.56

precipitates. Many coarse, secondary γ' precipitates surrounding the MC carbides partially dissolved. The first shape changes are observed at 950 °C, which occur over an increasingly larger area with increasing temperature. After heat treatment at 1100 °C, the “Chinese script” carbides are no longer fully surrounded by large γ' precipitates. There are fine precipitates at the grain boundaries, which in the initial state are M_5B_3 borides (Figure 7).^[27] They are still local and do not form continuous layers. The annealing exposure used in the experiments did not exceed their equilibrium solvus temperature estimated using the simulation.

The brief characterization of the microstructural changes presented above indicates that special attention should be paid to γ' precipitates behavior. The substantial variation in the size and morphology of the γ' precipitates (especially primary γ' and large eutectic γ/γ' islands) in the interdendritic regions and close to grain boundaries prevents the quantitative analysis of changes caused by short-term annealing. One factor that influenced the differences is the initial chemical composition of the γ' precipitates in dendrite cores and interdendritic regions, which, in turn, influences their thermodynamic stability. For the René 108 superalloy, this was more deeply discussed in our previous work.^[27] As a result of

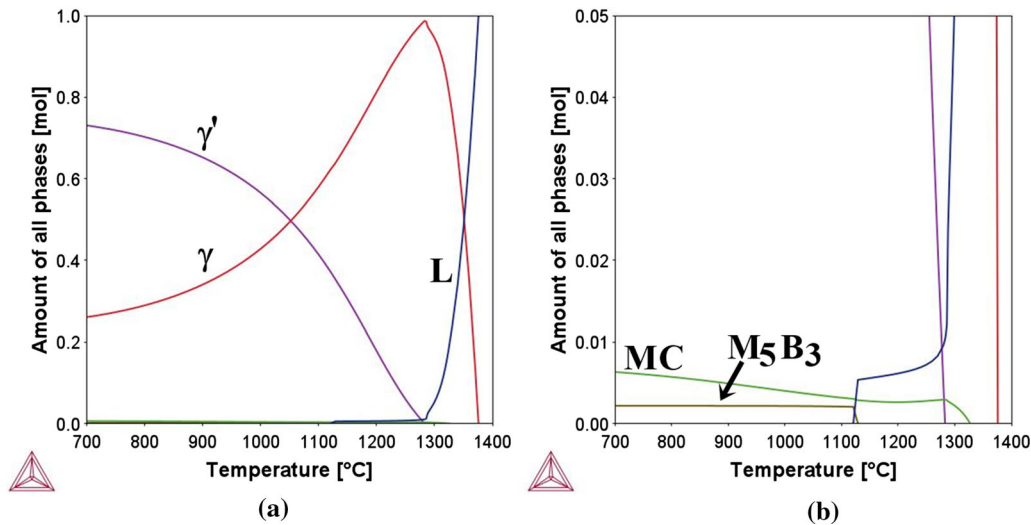


Fig. 3—Stability of strengthening phases with increasing temperature:(a) γ , γ' and L phases; (b) MC and M_5B_3 phases.

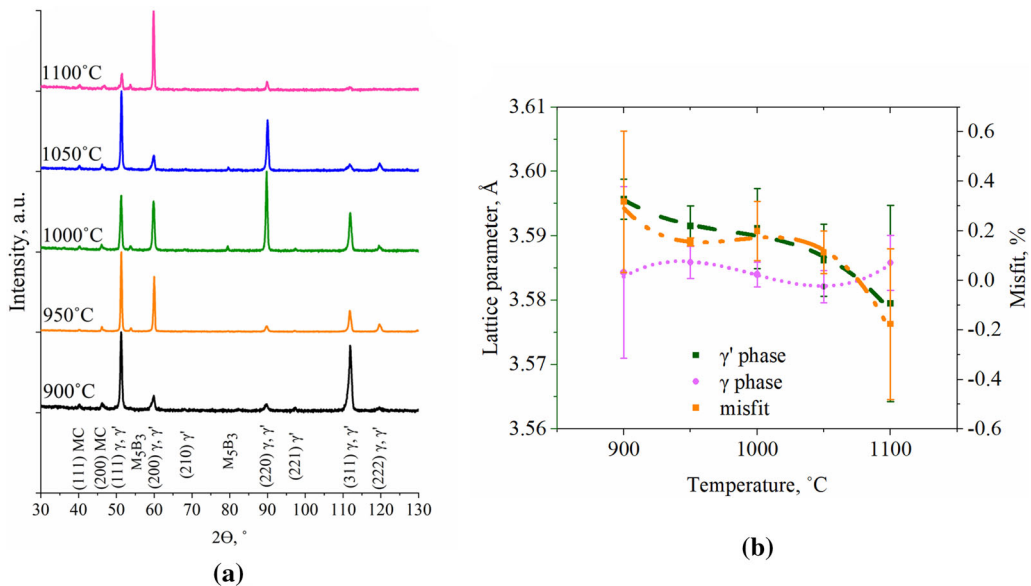


Fig. 4—(a) the XRD spectra of the René 108 superalloy after short-term annealing at 900-1100 °C; (b) influence of the short-term annealing temperature on the lattice parameters of the γ and γ' phases and misfit parameter. Calculated based on the XRD measurements and Nelson-Riley function.

aging, the initial microstructure of the dendrite cores is characterized by large γ' precipitates resulting from coalescence. Based on observations, it was found that dendrite cores are the representative areas for the analysis of the γ' precipitates dissolution process. In dendrite cores, the dissolution of γ' precipitates is more advanced than in interdendritic regions (Figure 8). The presented microstructures show the progressive dissolution of γ' precipitates, especially visible at 1050 °C, and 1100 °C. An obvious difference in dissolution can be observed for large secondary γ' precipitates to smaller ones with initially cubic (or close cubic) morphology. At the two highest temperatures, 1050 °C and 1100 °C, it is particularly evident that the number and size of large secondary γ' precipitates significantly decreased. In the case of smaller precipitates, the morphology remains almost the same; however, their size seems to change slightly. This indicates that large secondary γ' with complex morphologies are less stable than the finer secondary γ' with near-cubic shapes. This is particularly apparent when comparing the variance in γ' morphology at 950 °C and 1000 °C, where it can be concluded that the γ' dissolution does not go through the uninterrupted thinning of each γ' precipitate. A similar approach has been presented by Grosdidier *et al.*^[35,36]

Generally, the reduction of the system's internal energy drives the microstructural evolution in complex alloys like Ni-based superalloys. The (Eq. [6]) can express the energy state (E_{total}) of the single coherent γ' precipitate.

$$E_{\text{total}} = E_{\text{str}} + E_{\text{surf}} + E_{\text{int}} \quad [6]$$

where E_{str} elastic strain energy caused by the lattice misfit between γ' precipitate and γ matrix; E_{surf} surface energy (interfacial energy) of the γ' precipitate; E_{int} elastic interaction energy between γ' precipitates.

It has been experimentally confirmed that the γ' dissolution is also strongly influenced by the elastic field actions related to the misfit coefficient. The shape of the precipitates can evolve as the misfit increases, from sphere through cuboid to plates.^[37,38] The contribution of interfacial and elastic energies are of the same order of magnitude. The E_{surf} density is about 8 mJ m⁻², which for cubic precipitates with an edge of 0.5 μm is 1.2×10^{-11} mJ and is quite a low value relative to other systems.^[39] The elastic contribution impact depends on several factors, namely the mentioned misfit, the volume fraction of the γ' precipitates, their size and distribution in the matrix. Hazotte and Denis^[40] indicated, based on simulations, that the E_{int} of 10 pct cubic precipitates with a 0.5 μm edge length is estimated to be 3.5×10^{-11} mJ. Minimizing the elastic energy is a major driving force for microstructural evolution. It can be realized through different ways: (1) the local redistribution of solute atoms, (2) decrease in coherency and pinning of dislocations of the γ/γ' interface, (3) change in γ' precipitate morphology, their arrangements, and movement of the γ/γ' interface. The two first can coexist during the short-term exposure of the René 108 alloy. Despite the substantial reduction in elastic energy by

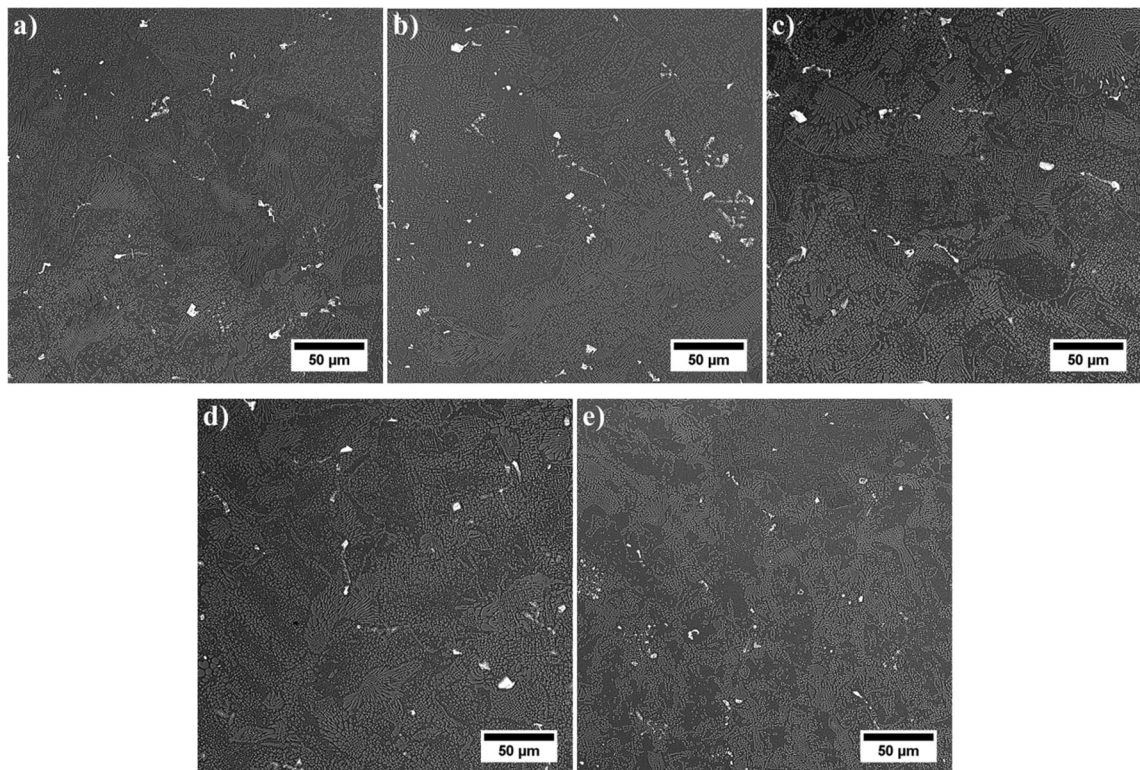


Fig. 5—Dendritic structure of the cast superalloy and distribution and morphology of MC carbides after annealing at (a) 900 °C; (b) 950 °C; (c) 1000 °C; (d) 1050 °C; and (e) 1100 °C, SEM-BSE contrast.

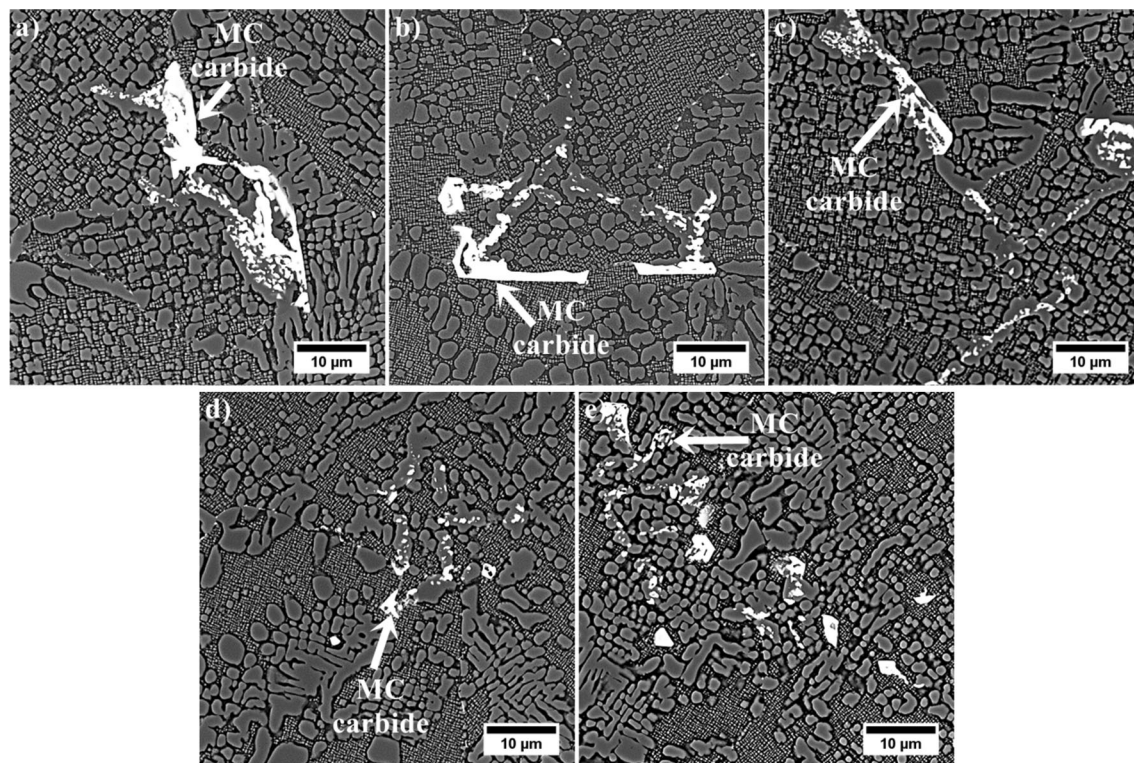


Fig. 6—Morphology of the MC carbides and γ' precipitates in the interdendritic region after annealing at (a) 900 °C; (b) 950 °C; (c) 1000 °C; (d) 1050 °C; and (e) 1100 °C, SEM-BSE contrast.

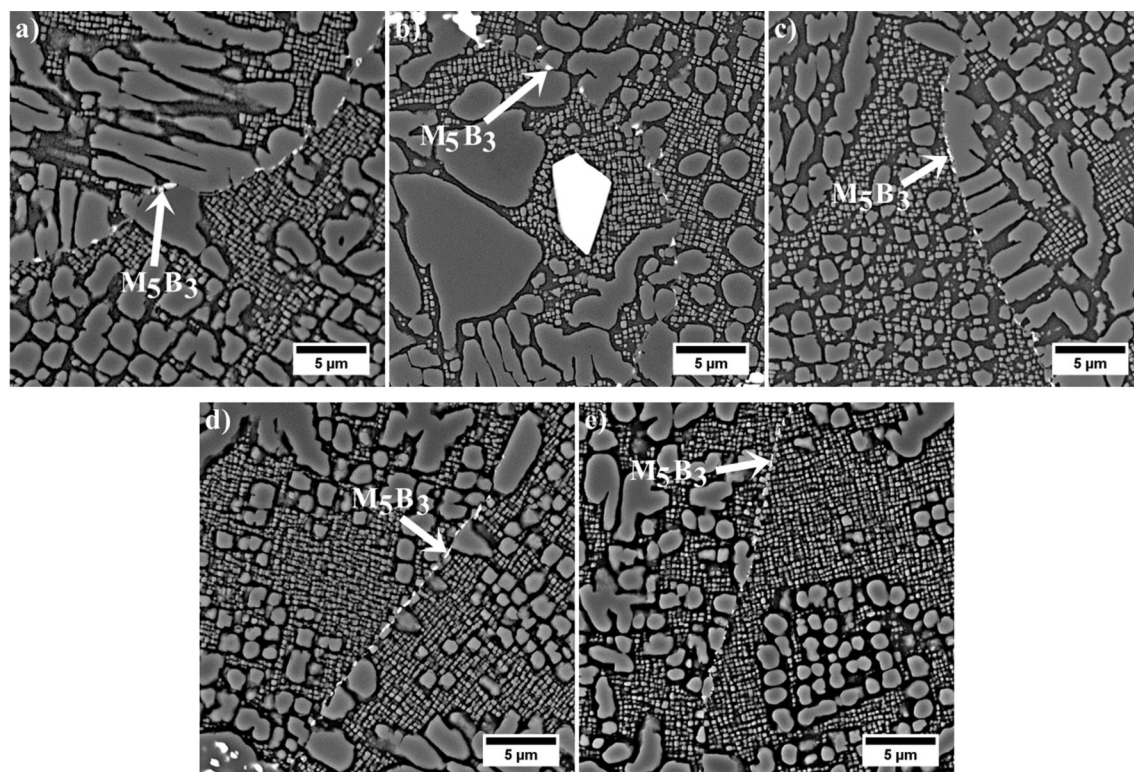


Fig. 7—Morphology of the M_5B_3 precipitates at the grain boundaries after annealing at (a) 900 °C; (b) 950 °C; (c) 1000 °C; (d) 1050 °C; and (e) 1100 °C, SEM-BSE contrast.

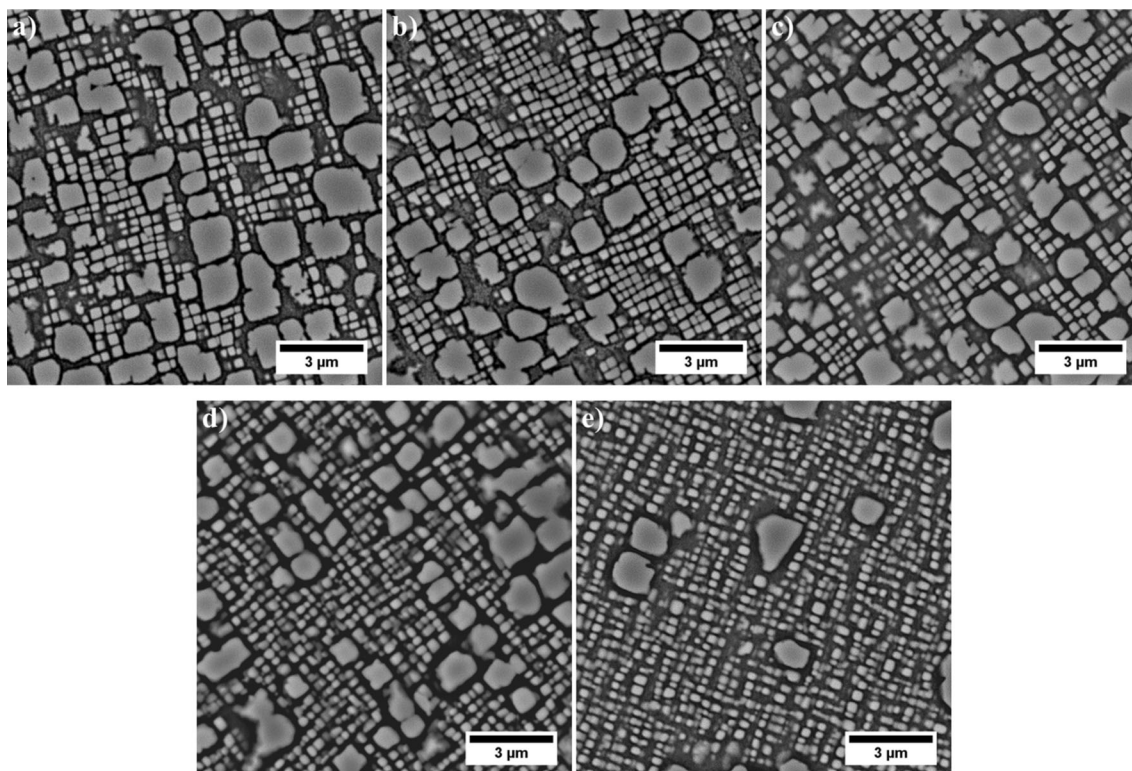


Fig. 8—Morphology of the γ' precipitates in the dendrite cores after annealing at (a) 900 °C; (b) 950 °C; (c) 1000 °C; (d) 1050 °C; and (e) 1100 °C, SEM-BSE contrast.

plastic relaxation accompanied by a decrease in coherency, it can usually have a strong influence when Ni-based superalloys are subjected to prolonged aging or plastic deformation.^[41,42] The conditions in our experiments did not create such favorable conditions for these changes. The last are important when the precipitates are keeping coherency with a matrix. The microstructural evolution is affected by the strong elastic anisotropy between γ' and γ , while $\langle 001 \rangle$ directions are the softest.^[43] The equilibrium morphology is an outcome of the balance between interfacial and elastic energy contributions. The first one is proportional to the γ/γ' interface area and favor compact, isotropic precipitate shapes.^[35] The second is proportional to the γ' precipitate volume and tends to promote faceting along the softest planes $\{001\}$. The elastic interaction arises from the overlap of the individual γ' precipitates strain fields when the distance between them is small.^[44] The elastic anisotropy factor (A) in superalloys is greater than unity. Consequently, the interaction energy between two γ' precipitates takes a negative minimum if they are adjacent to each other along the $\langle 001 \rangle$ directions.^[45] From an elastic point of view, elastically constrained coherent γ' precipitates are more stable when aligned along the $\langle 001 \rangle$ directions than along the $\langle 011 \rangle$ or $\langle 111 \rangle$. The differences in local stability connected with the elastic interactions decide which precipitates start to dissolve first. If the γ' precipitates are “kept” by elastic interactions, the dissolution process is realized via the gradual disappearance of these precipitates which are being

unstable.^[35] The morphology of γ' precipitates is determined by minimizing the sum of the precipitate elastic strain energy, the precipitate surface energy, and the elastic interaction energy between precipitates.^[46–48] Balancing of internal energy occurs continuously at each temperature. It should be emphasized that the equilibrium state at temperature *no. 1* will not also be equilibrium at temperature *no. 2*. Additionally, the equilibrium chemical composition at the γ/γ' interface also changes with increasing temperature. Large secondary γ' precipitates with a significant curvature interface will tend to obtain a smooth interface.

The large secondary γ' precipitates were unstable at high temperatures and were partially dissolved with the formation of several split patterns, as presented in Figure 9. Precipitate splitting in Ni-based superalloys is most likely to occur for cuboidal γ' precipitates, where there is a relatively large δ parameter. High elastic strain energy can cause morphological instability and, consequently, the γ' precipitates divide into finer γ' precipitates to decrease the total energy of the system.

In a situation, where we use the common concept that the precipitate shape can be described by the sum of elastic strain energy and the surface energy, the phenomenon of splitting cannot be accounted for. This is due to the total energy of the precipitate significantly increasing with the increase in the surface area induced by splitting. However, the presented γ' precipitate morphologies confirm that splitting took place during short-term annealing of the René 108 alloy. This indicates that some processes coexists, which leads to a

decrease in the total energy by overcoming an increase in the surface energy. This process is elastic interaction energy, which can be analyzed as the influence of a single precipitate. The comparison of the total energy of the γ' precipitate before ($E^{(1)}$) and after the splitting into eight fine precipitates ($E^{(8)}$) has been investigated by Doi.^[38] The horizontal line in Figure 10 corresponds to the diameter of individual γ' precipitate before splitting. When the precipitate size is small, the total energy $E^{(1)}$ is lower than $E^{(8)}$, therefore it is stable and more favorable is its existence as a single precipitate. If the precipitate starts to grow, the energy $E^{(8)}$ tends to be lower than energy $E^{(1)}$, and then the energetically favorable shape is an octocube (ogdoad) instead of a single precipitate. Octocube in the cross-sectional view can be represented as a quartet split pattern. The elastic interaction causes a significant contribution to the reduction in total energy, leading to splitting. Based on the common concept that the shape of the precipitate is established by the sum of the elastic strain energy and the surface energy, the total energy increases from A to A'' . This happens as the surface area is larger due to splitting, while the elastic interaction energy is skipped. It should be noted that the elastic interaction really contributes to the determination of the stable shape of the γ' precipitates. As presented in Figure 10, the γ' precipitate attempts to reduce the total energy from A to A' and this leads to splitting into the stable shape, octocube.

Vogel *et al.*^[49] has also confirmed that the strong elastic constraints between neighboring γ' precipitates lead to a decreased size during aging treatment (large secondary γ' precipitates $\xrightarrow{\text{splitting}}$ fine cuboids). Energetically, splitting of the γ' precipitates is beneficial when the drop in the system elastic strain energy more than compensates for the increase in formed interfacial energy. Large misfit generates high elastic strain, and the precipitates tend to split along the most elastically compliant direction. The microstructure of γ' precipitates presented in Figure 9 shows that the magnitude size of the elastic interaction energy related to the surface energy decides if the γ' precipitate are stable or split. Doi *et al.*^[38] proposed that the influence of the elastic interaction on the shape of precipitates can be predicted using (Eq. [7]).

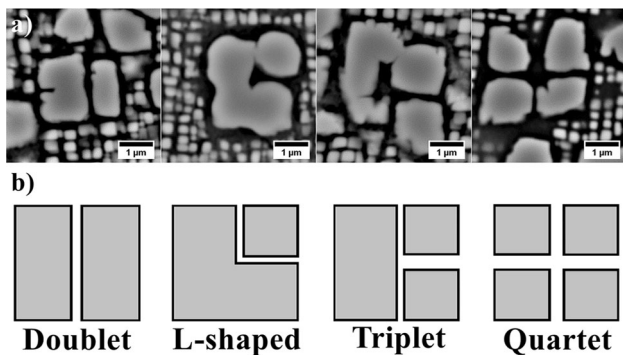


Fig. 9—Dissolution/decomposition of the γ' precipitates in the dendrite cores via the splitting mechanism: (a) imaged; (b) schematic, SEM-BSE contrast.

$$\Delta^* \equiv \frac{\delta}{\gamma_s} = \frac{e^{T^*}}{\gamma_s} = \frac{a_{\gamma'} - a_{\gamma}}{a_{\gamma}} \cdot \frac{1}{\gamma_s}, \text{ m}^2 \text{ J}^{-1} \quad [7]$$

where $\delta = \gamma/\gamma'$ misfit, γ_s —surface energy density, e^{T^*} —eigenstrain (stress-free strain), a_{γ} and $a_{\gamma'}$ —lattice parameters of the γ and γ' phases calculated based on method proposed by Watanabe and Kuno^[50].

When the $|\Delta^*|$ is lower than 0.2, the precipitate remains spherical and does not split. If $0.2 < |\Delta^*| < 0.4$, the cuboidal precipitate tends to split into eight cuboids (ogdoad). A precipitate splits into a two precipitate (doublet) when the absolute value of $|\Delta^*|$ is equal or higher than 0.4. As the $|\Delta^*|$ tends to be higher, the precipitate size, at which the splitting occurs, becomes finer.

Grosdidier *et al.*^[35] indicated that the morphological transformations sphere→cube→octocube are very fast since the process is controlled by an interfacial reaction. The frequency of atomic jumps through the interface is essential rather than long distance diffusion. Several authors^[51–54] noticed that even in simple model alloys, the evolution of the γ' precipitates morphology during aging and heat treatment is not uniform and exhibits differences controlled by many factors. It is worth noting the results by Chen *et al.*^[55] who observed an anomalous cyclic coarsening behavior of secondary γ' precipitates during aging of RR1000 superalloy. The microstructure evolved with repeating cycle, namely the instability of the precipitates→splitting→growth. The dissolution of γ' precipitates could be more continuous and uniform in the absence of a sufficiently high elastic strain field. It was noticed that some voids within large secondary γ' precipitates may occur (Figure 11), although this was not observed in for the alloy's initial state. Their presence may be an effect of the cross-sectioned precipitate observations; however, as many precipitates have a regular shape close to spherical, this suggests that some microstructural changes occurred there.

Vogel *et al.*^[56] proved that local chemical composition fluctuations occur inside the γ' precipitates, with the formation of the γ phase, making the hierarchial microstructure $\gamma_{\text{matrix}} \subset \gamma'_{\text{precipitate}} \subset \gamma_{\text{precipitate}}$. When

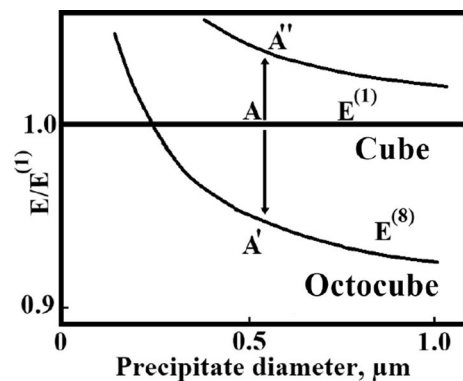


Fig. 10—Comparison of the total energy of the γ' precipitates before and after the splitting into eight fine precipitates. From Ref. [38] with permission.

such γ reaches the γ' interface, their splitting would be observed. This conclusion is in line with our observation. Vogel *et al.*,^[49] based on the statistical analysis of three-dimensional atom probe data concluded that the temperature-dependent solubility of Ni might explain the initial decomposition within the γ' precipitate. Its concentration in the γ' phase tends to be lower with decreasing temperature due to local equilibrium state between γ' and dual-phase $\gamma + \gamma'$ area. Supersaturation in Ni is the driving force for γ phase separation. Despite extensive surface and, thus, molar surface energy (E_m) are formed, Ni's enrichment supports Ni-rich clusters creation, as this locally decreases the molar free energy. The decomposition of the γ' phase leads to the formation of the Ni-rich and Ni-depleted clusters and can be explained as initial stages of γ precipitation in the γ' phase. Coalescence of Ni-rich clusters leads to the formation of γ spheres and the surface energy is considerably reduced.^[56] This has been observed in the model Ni-Al-Ti alloy after aging at 750 °C. The γ spheres are metastable and evolve to the equilibrium γ phase, entailing a morphological transformation from spheres to plates. The elastic energy's relative gain to interfacial energy, which increases with the precipitate size is leading to this morphology evolution.^[46] The obtained γ plates stay aligned with the elastically soft directions of the γ' precipitates, making this energetically favorable due to the presence of elastic interactions between the precipitates.^[57] Via the morphological change spheres→plates, the γ phase achieves equilibrium composition. The γ precipitates inside the γ' phase increases shearing resistance of the γ' , as confirmed by Tian *et al.*^[58]

To quantify the dissolution process in the René 108 alloy, the analysis of the stereological parameters of the γ' precipitates in the dendrite cores was performed. Figure 12 shows that the mean surface fraction of the measured γ' precipitates gradually decreased with increasing annealing temperature from 0.52 to about 0.34 at 1100 °C.

Based on a γ' dissolution study, Giraud *et al.*^[11] have shown that during the initial transient stage ($t < 1$ minute) of the annealing at 1200 °C, the dissolution process progresses rapidly. A spectacular 25 pct

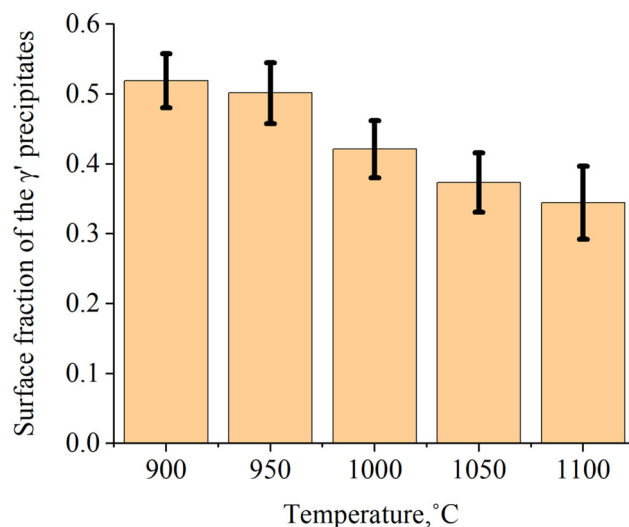


Fig. 12—Influence of short-term annealing temperature on the surface fraction of the γ' precipitates in dendrite cores.

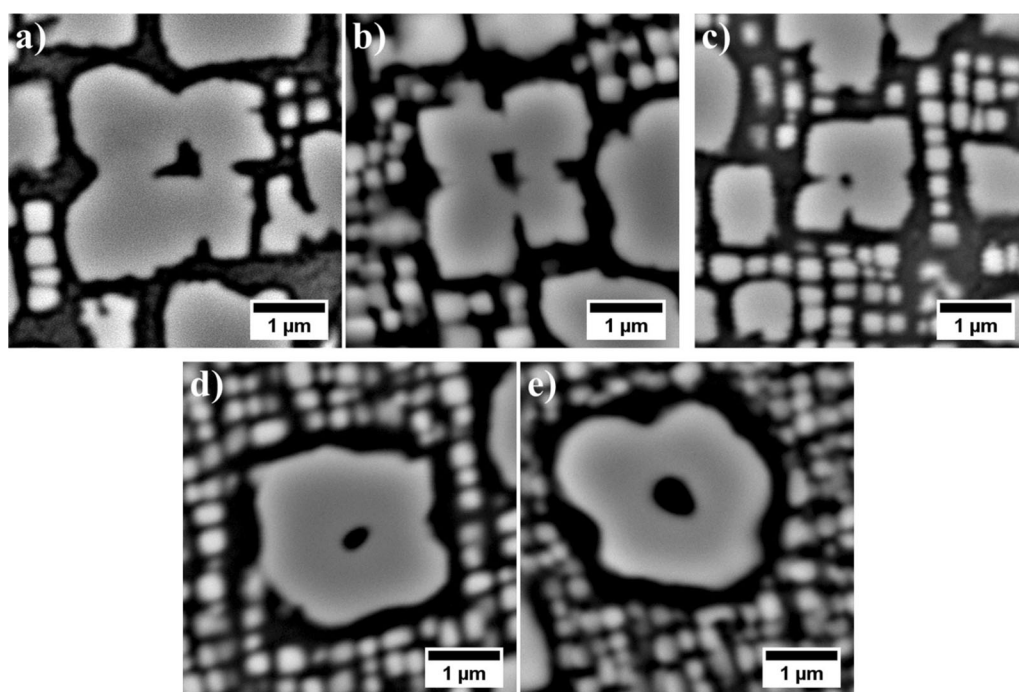


Fig. 11—Decomposition within the γ' precipitates after annealing at (a) 900 °C; (b) 950 °C; (c) 1000 °C; (d) 1050 °C; and (e) 1100 °C, SEM-BSE contrast.

decrease in γ' volume fraction was noted. A second stage, observed between 1 to 15 minutes, corresponded to the curvature of the dissolution kinetics directly before reaching the equilibrium value. Only after this time, the values were in good agreement with the ThermoCalc predictions. This allows to conclude that the results presented in Figure 12 can be included in the second stage, where the equilibrium state is yet achieved and the deviation from the thermodynamical simulation is present. Since the dissolution is diffusion controlled, the much longer annealing dwell time of the René 108 is required to obtain the volume fraction of γ' calculated with simulations.

The mean size of γ' precipitates expressed as the equivalent diameter was calculated to quantitatively analyze the microstructural changes caused by high temperature exposure. Figure 13 shows the distribution of the equivalent diameter of the γ' precipitates and fitted curves representing log-normal distribution. At

900 °C, two curves corresponding to an average size of $\bar{\phi}_1 = 0.37 \mu\text{m}$ and $\bar{\phi}_2 = 1.06 \mu\text{m}$, are presented. At 950 °C, curve $\bar{\phi}_1$ is shifting to the right to 900 °C, i.e., toward higher values, whereas curve $\bar{\phi}_2$ to lower. It may indicate that large γ' precipitates partially dissolve and are included in the distribution corresponding to curve $\bar{\phi}_1$. Simultaneously, fine γ' precipitates slightly increase in size due to the increase in the frequency of precipitates with a diameter of 0.3 to 0.5 μm . From 950 °C to 1000 °C, the value of $\bar{\phi}$ drops for two curves and increases the finer precipitates' frequency. Dissolution, as a dominating process, is also continued at two subsequent temperatures. So much so that at 1100 °C, only one curve of the size distribution is fitted to the histogram. The data summarized in cumulative curves clearly show that the fraction of large secondary γ' precipitates is the highest at 900 °C, their contribution decreases with a increasing annealing temperature. The surface fraction of precipitates with $\bar{\phi} \geq 0.4 \mu\text{m}$

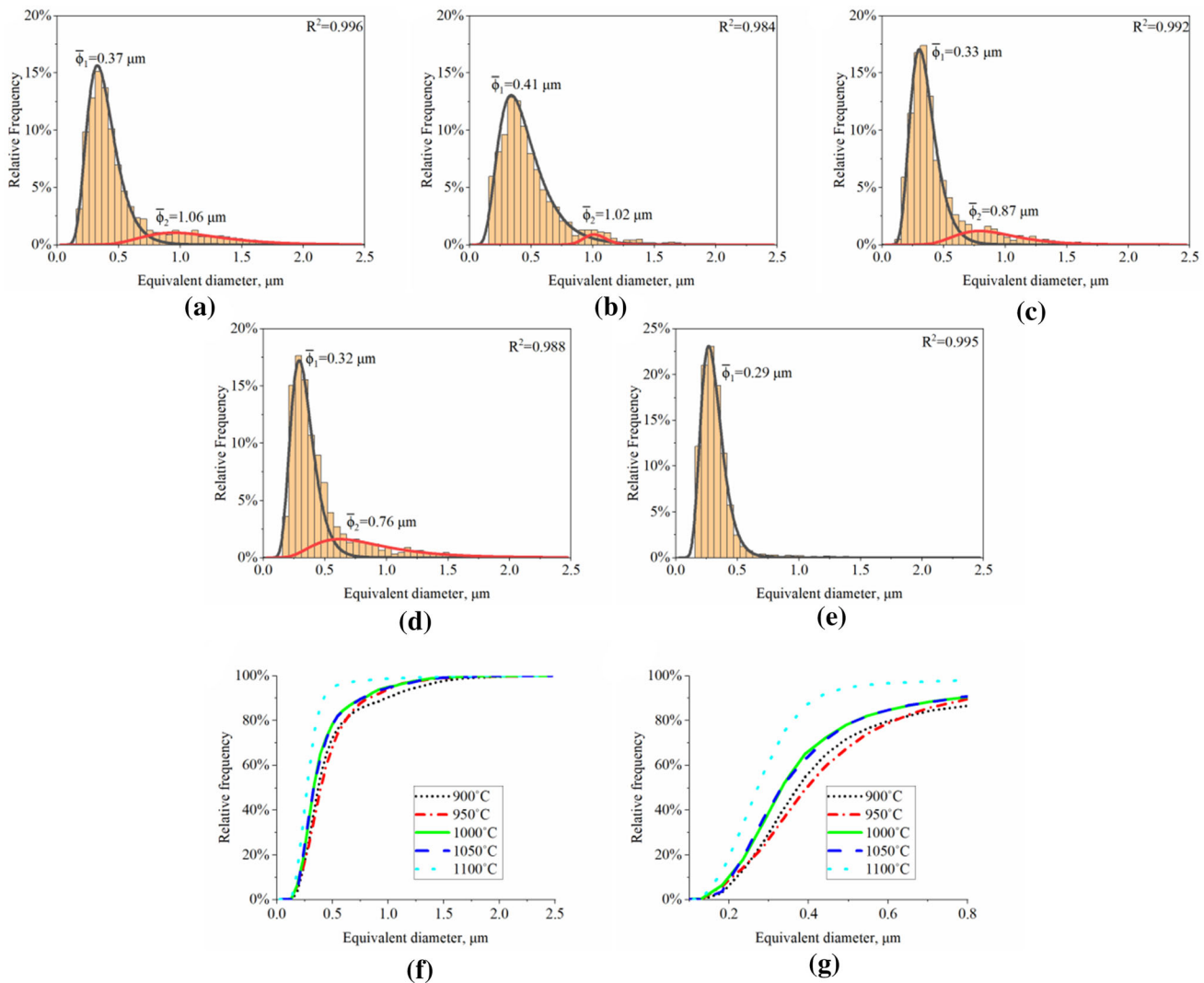


Fig. 13—Influence of annealing temperature on the equivalent diameter distribution: (a) 900 °C; (b) 950 °C; (c) 1000 °C; (d) 1050 °C; and (e) 1100 °C; (f, g) cumulative curves. Red and black continuous lines represent bimodal distribution with two distinct precipitates populations (Color figure online).

decreases gradually with increasing temperature from 900 °C to 1050 °C (Figure 14).

At 1100 °C, the decrease is more pronounced, which indicates that at the moment the splitting of large precipitates is most advanced. The presented results show that during annealing, not only precipitates dissolution, but also local precipitates coagulation can take place. These observations are the result of the

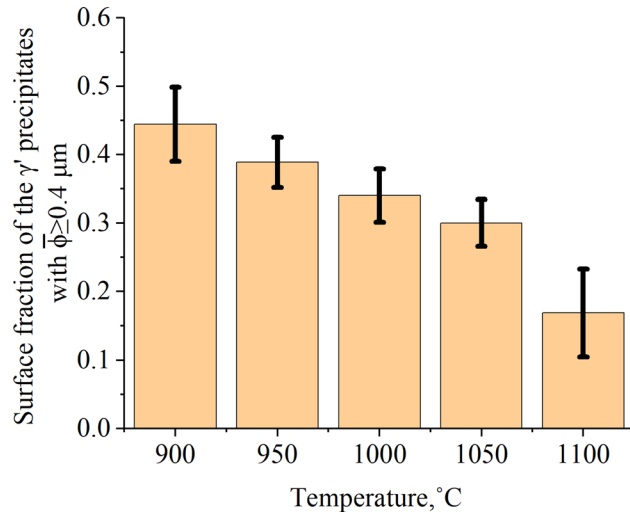


Fig. 14—The surface fraction of the γ' precipitates with $\bar{\phi} \geq 0.4 \mu\text{m}$ in dendrite cores.

influence of the coexistence and interaction of both processes, with the increase in temperature making dissolution the prevailing one.

The circularity was calculated to reveal the change of the γ' precipitates morphology (Figure 15). Generally, the perfectly spherical precipitates have a $\zeta = 1$, while cubic $\zeta = 0.785$. Data are summarized as a histogram. As the temperature increases from 900 °C to 950 °C, the frequency of the precipitates with a $\zeta \geq 0.785$ increases, which suggests the simultaneous contribution of the dissolution of large γ' precipitates and coarsening of smaller ones. At 1000 °C and 1050 °C, the frequency of the precipitates with a $\zeta \geq 0.785$ gradually decreases, which can be derived from the splitting of large γ' precipitates and changing of smaller precipitates from cubic- to elongated cuboidal shaped. The number of precipitates with a ζ around 0.6 increases after annealing at 1100 °C, which corresponds to partially dissolved large γ' precipitates and many precipitates with elongated cuboidal shaped.

D. TEM Investigation of Microstructural Changes of the Superalloy After the Short-Term Annealing at 1100 °C

Samples characterized by the most progressive changes induced by the dissolution process (after the annealing at 1100 °C) were investigated by TEM. At the interfaces of the matrix with secondary γ' precipitates, numerous dislocations and an extensive dislocation network are present (Figures 16(a), (b)). Dislocation movement and increased dislocation density occurred

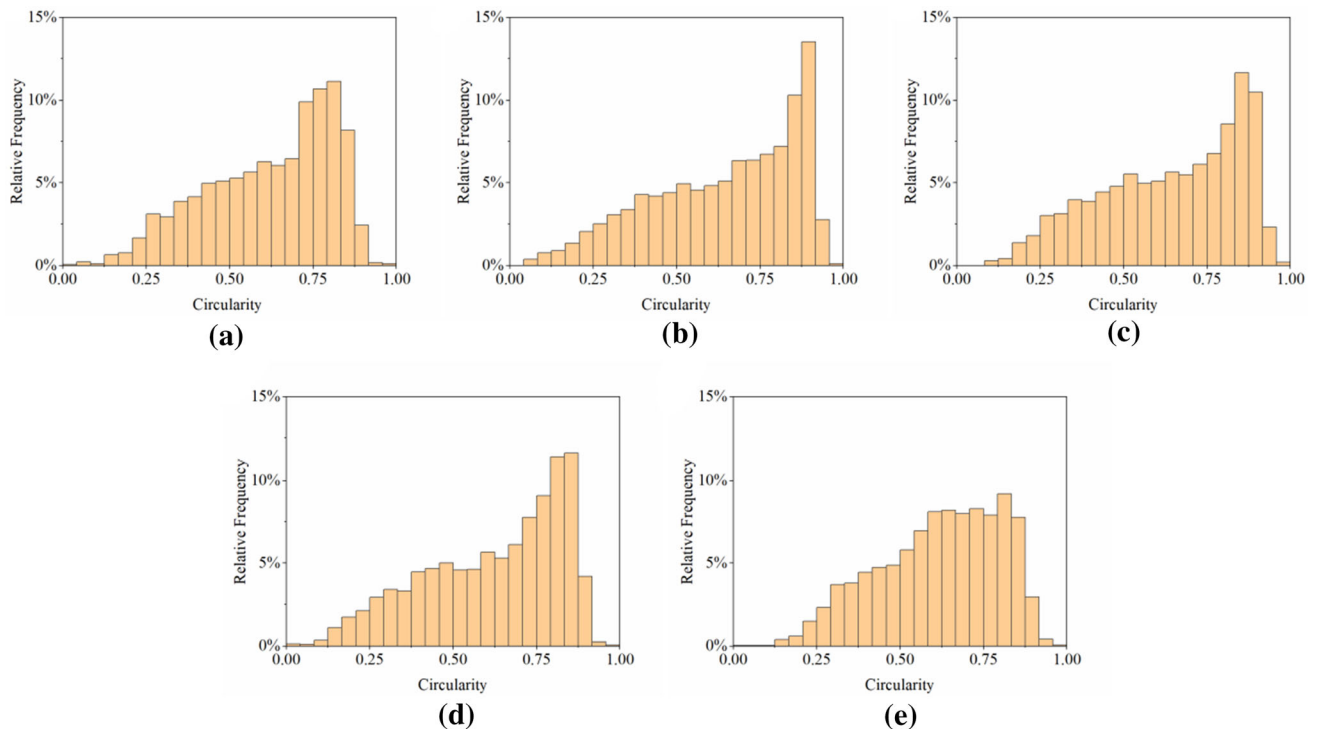


Fig. 15—Influence of the heat treatment temperature on the circularity of the γ' precipitates: (a) 900 °C; (b) 950 °C; (c) 1000 °C; (d) 1050 °C; and (e) 1100 °C.

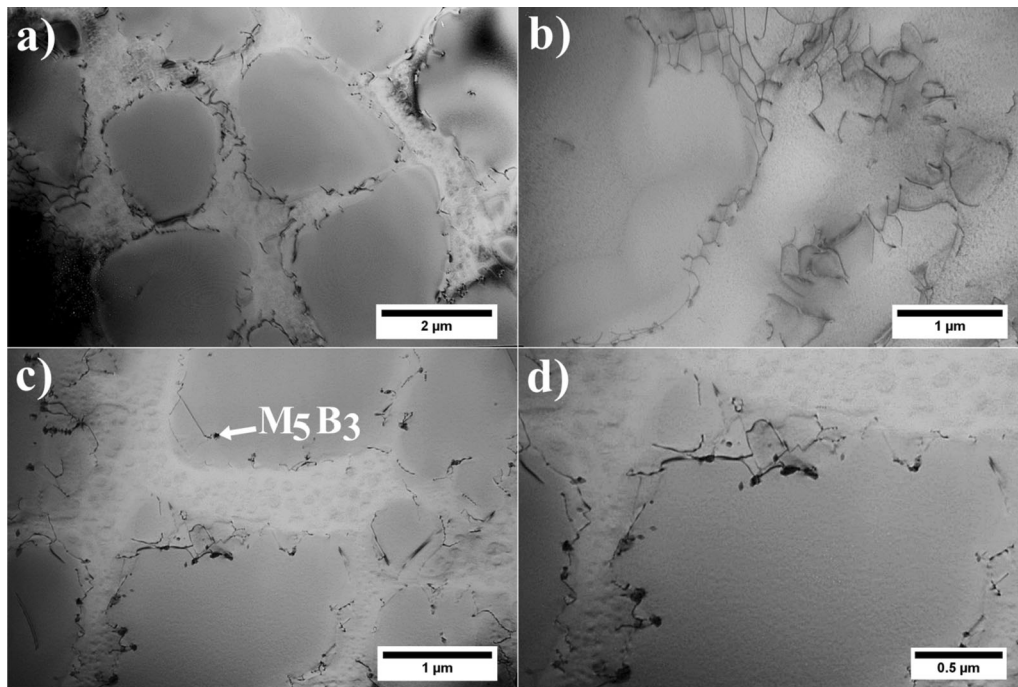


Fig. 16—Morphology of the γ' precipitates and structural defects after annealing at 1100 °C: (a), (b) large γ' precipitates and dislocation networks in the dendrite cores; (c) and (d) nanoborides at the γ/γ' interfaces, TEM-BF.

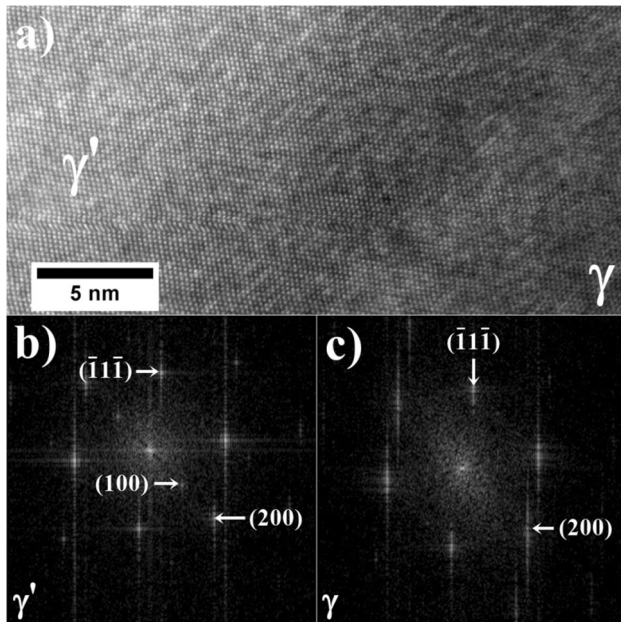


Fig. 17—(a) nanostructure of the γ' and γ ; (b) and (c) diffraction patterns of the γ and γ' phases. Zone axis $[011]_{\gamma}$, HAADF-STEM.

during short-term annealing in the absence of external load and was driven by the demand to relax strain fields originated from lattice misfit. The mobility of the γ/γ' interface changes during annealing. The formed dislocation networks accommodate the lattice misfit between the γ and γ' phases. The images confirm that the difference in lattice parameter between phases influences the interface nature and morphology of the γ'

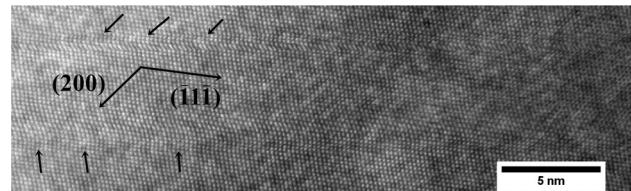


Fig. 18—Stress accommodation in the γ' precipitate and γ matrix, HAADF-STEM.

precipitates. The M_5B_3 nanoborides, which were present locally at the γ/γ' interface in the initial state, remained stable (Figures 16(c), (d)). They occur in the form of single precipitates and constitute an additional obstacle for dislocation movement and γ/γ' interphase mobility during annealing. At the edges of the cubic precipitates, dislocations and dislocation networks are missing, which suggests much lower misfit stresses. This is also the case for γ' nanoprecipitates, which formed during cooling from the saturated matrix.

The γ/γ' interfaces for secondary γ' precipitates were also investigated at the atomic scale using the HAADF-STEM technique (Figure 17). Images were captured with an incident beam parallel to the $\langle 011 \rangle$ crystallographic orientation. The HAADF-STEM image revealed interplanar distances to be similar both for the γ matrix and coherent γ' precipitates. Individual diffraction peaks for γ and γ' phases were obtained by FFT of the nanostructure. For the face-centered cubic (FCC) Ni matrix phase, the $\{200\}$ and $\{\bar{1}1\bar{1}\}$ reflections revealed that for the ordered $L1_2$ structure of the γ' phase the $\{100\}$ superlattice reflections are also present. Elastic distortion of the matrix arising from coherent

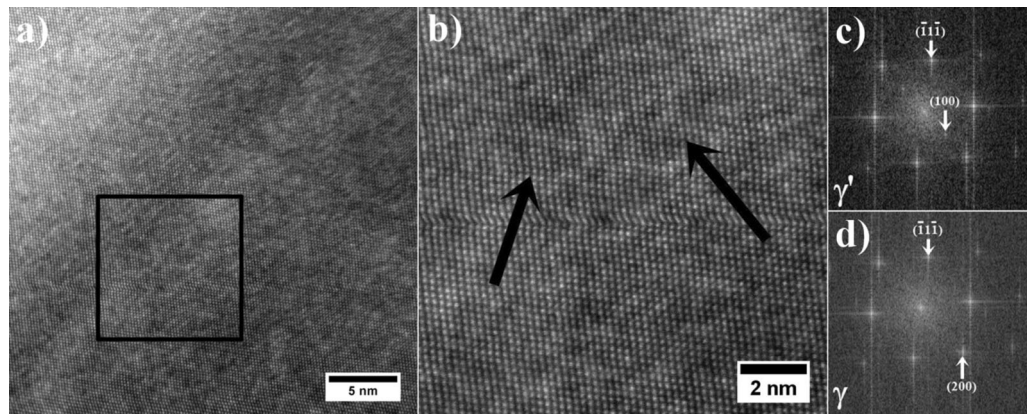


Fig. 19—(a) and (b) the γ' nanoprecipitates at the γ/γ' interface; (c) and (d) diffraction patterns of the γ' nanoprecipitates and γ . Zone axis $[011]_{\gamma, \gamma'}$, HAADF-STEM.

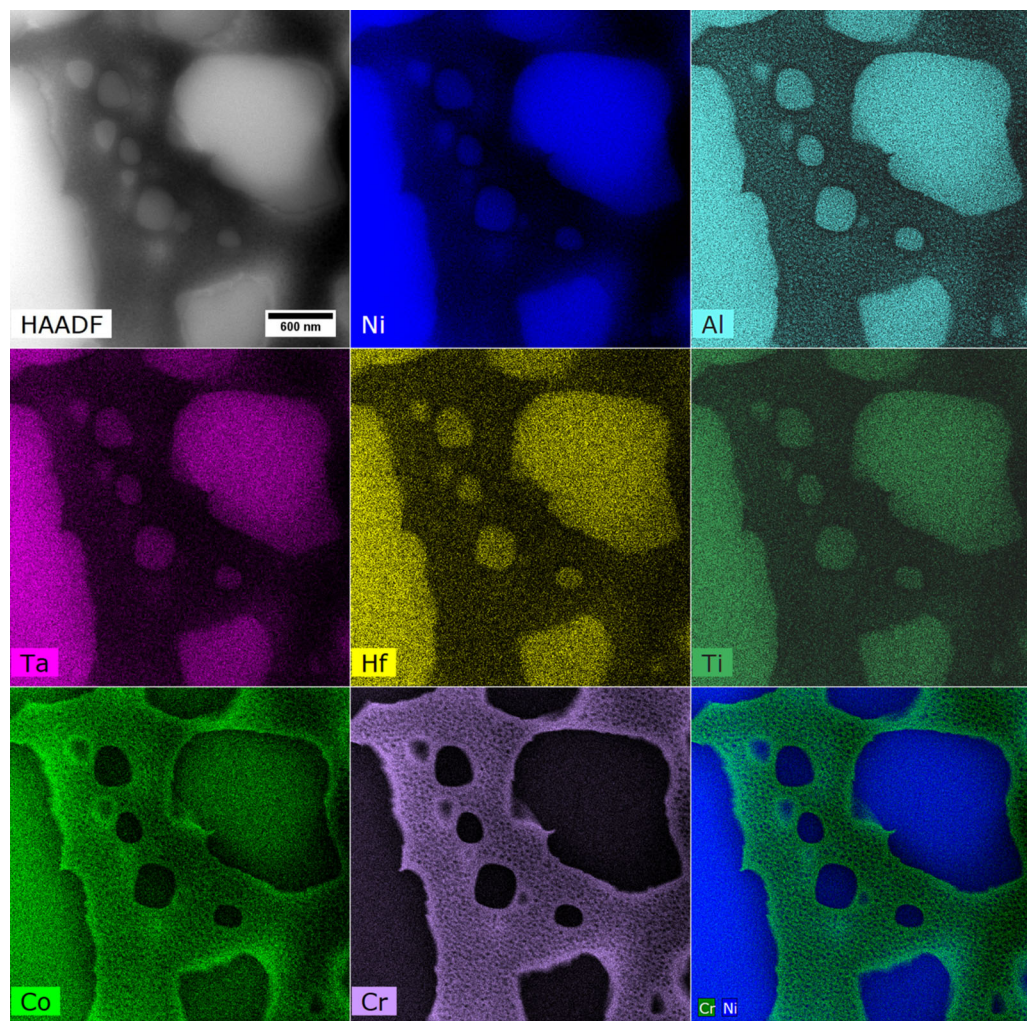


Fig. 20—Distribution of selected alloying elements in the γ matrix and γ' precipitates in the dendrite cores, STEM-EDX.

misfitting precipitate produces diffuse scattering in reciprocal space in the direction of the distortion. Numerous regions indicating stress accommodation

(indicated with arrows) by the γ' precipitates and the γ matrix have been found (Figure 18). The locally observed shift of atomic columns is around 0.09 Å.

Detailed analysis of the γ/γ' interfaces revealed γ' nanoprecipitates with a size around 2 to 3 nm which were formed from saturated matrix (enriched in γ' -formers) during cooling after annealing (Figure 19). The presence of similar γ' nanoprecipitates has also been confirmed by Penkala *et al.*^[59] based on the observation of the Waspaloy superalloy in atomic-scale resolution.

The STEM-EDX distribution maps of selected alloying elements were performed in the dendritic area (Figure 20). The regions enriched in Ni, Al, Ti, Ta, and Hf correspond to γ' precipitates, while those enriched in Cr and Co correspond to the matrix. Within the γ matrix close to the γ/γ' interface, enrichment in Co and Cr and low levels of depletion in Al were revealed. This confirms the presence of a diffusion zone and that the diffusion processes participated in the dissolution of γ' precipitates. Segregation of alloying elements in the close proximity to the interface strongly influences on the local misfit changes. Most alloying elements diffuse orders of magnitude faster in the γ matrix (FCC) than within the ordered intermetallic $L1_2$ structure of the γ' precipitates.^[60,61] The matrix area near the γ/γ' interface may become a bottleneck for diffusion, leading to diffusive interfaces. Wide diffusive interfaces can be formed when the γ/γ' interfacial energy is extremely low (around 10 mJ/m²).^[62] A similar distribution of Cr, Co, and Al (also Ti) close to the γ/γ' interface was observed by Chen *et al.*^[55] during the study of the aged RR1000 superalloy. In the presented maps, depletion in Ti is not visible, probably due to low its initial concentration. Campbell *et al.*^[63] showed that in Ni-based superalloys, Co has a negative chemical interdiffusivity if other elements, such as Cr, Al, and Ti are present. Consequently, Co enrichment at the γ/γ' interface will slow down Cr and Al interdiffusion as compared to γ phase regions far from the interface. It could, therefore, cause the depletion in Al close to the interface. The depletion of γ' -former near the γ/γ' interface will have a further effect of slowing down the growth of γ' . It could, in turn, explain the absence of significant growth of secondary γ' precipitates during annealing. Campbell's interdiffusion matrix also predicts that a lower concentration of Al and Ti (γ' -formers) will slow down Co diffusion. Therefore, more time is required to homogenize Co at the γ/γ' interface. The images confirm that during rapid cooling, the γ' nanoprecipitates were reprecipitating from the matrix.

IV. CONCLUSIONS

Based on the above presented results, the following conclusions are proposed:

1. For all annealed samples, XRD spectra revealed that the obtained peaks correspond to four phases: matrix γ , intermetallic γ' , MC carbides, and M_5B_3 borides. The γ/γ' misfit parameter (δ) was positive for 900 °C to 1050 °C and negative for 1100 °C. Its value changes with increasing temperature, from + 0.32 to – 0.18 pct at 1100 °C.

2. Short-term annealing leads to the dissolution of γ' precipitates. The mean surface fraction of the secondary γ' precipitates in dendrite cores decreased from 0.52 at 900 °C to 0.34 at 1100 °C.
3. The dissolution of γ' precipitates does not proceed through uninterrupted thinning of each precipitate due to local stability differences, which originate from elastic interactions. The process was found to be strongly affected by the presence of an elastic strain field associated with the γ/γ' misfit.
4. Large secondary γ' precipitates dissolved through splitting and consequently formed various splitting patterns.
5. Histograms of the equivalent diameter of precipitates ($\bar{\phi}_i$) curves representing their size were fitted by log-normal function. At 900 °C, the $\bar{\phi}_1$ and $\bar{\phi}_2$ are equal to 0.37 and 1.06 μm , respectively. Increasing the temperature to 950 °C led to the overlapping of dissolution and local coarsening, as $\bar{\phi}_1$ and $\bar{\phi}_2$ slightly changed to 0.41 and 1.02 μm , respectively. For higher temperatures, dissolution was the predominant process. At 1100 °C, only one curve could be fitted, namely, $\bar{\phi}_1 = 0.29 \mu\text{m}$. Still, large secondary γ' precipitates were present; however, they constituted only a small volume fraction.
6. The ζ coefficient representing precipitate shape confirms the complexity of the microstructural changes. From 900 °C to 950 °C, the increase in precipitate fraction with $\zeta \geq 0.7$ indicated that some of them tend to have a cubic or spherical morphology. At higher temperatures, the non-continuous thinning of γ' induced by the dissolution process caused an increase in the number of precipitates with more complex shapes (lower ζ).
7. At the γ/γ' interfaces in samples annealed at 1100 °C, numerous dislocation networks were revealed. At the γ/γ' interfaces, the M_5B_3 nanoborides were still present and act as an obstacle for interface mobility.
8. The STEM-EDX mapping of the alloying elements in the dendrite cores revealed the Cr and Co-enriched and Al-depleted areas close to the γ/γ' interfaces. It is assumed based on the literature that the Co enrichment at the γ/γ' interface could slow down the interdiffusion of Cr and Al as compared to γ phase regions far from the interface and could, therefore, cause the depletion in Al close to the interface.

ACKNOWLEDGMENTS

This work was supported by the Polish National Science Centre (Preludium 13) under grant 2017/25/N/ST8/02368. The authors wish to express appreciation to prof. Wiktoria Ratuszek (AGH-UST) for supporting the XRD study.

CONFLICT OF INTEREST

The authors declare no conflict of interest.

OPEN ACCESS

This article is licensed under a Creative Commons Attribution 4.0 International License, which permits use, sharing, adaptation, distribution and reproduction in any medium or format, as long as you give appropriate credit to the original author(s) and the source, provide a link to the Creative Commons licence, and indicate if changes were made. The images or other third party material in this article are included in the article's Creative Commons licence, unless indicated otherwise in a credit line to the material. If material is not included in the article's Creative Commons licence and your intended use is not permitted by statutory regulation or exceeds the permitted use, you will need to obtain permission directly from the copyright holder. To view a copy of this licence, visit <http://creativecommons.org/licenses/by/4.0/>.

REFERENCES

1. R.C. Reed: *The Superalloys: Fundamentals and Applications*, Cambridge University Press, Cambridge, UK, 2006, pp. 1–28.
2. T.M. Pollock and A.S. Argon: *Acta Metall. Mater.*, 1992, vol. 40, pp. 1–30, [https://doi.org/10.1016/0956-7151\(92\)90195-K](https://doi.org/10.1016/0956-7151(92)90195-K).
3. T. Murakumo, T. Kobayashi, Y. Koizumi, and H. Harada: *Act. Mater.*, 2004, vol. 52, pp. 3737–44, <https://doi.org/10.1016/j.actamat.2004.04.028>.
4. S.V. Prikhodko and A.J. Ardell: *Act. Mater.*, 2003, vol. 51, pp. 5021–36, [https://doi.org/10.1016/S1359-6454\(03\)00328-8](https://doi.org/10.1016/S1359-6454(03)00328-8).
5. T.M. Pollock and A.S. Argon: *Acta Metall. Mater.*, 1994, vol. 42, pp. 1859–74, [https://doi.org/10.1016/0956-7151\(94\)90011-6](https://doi.org/10.1016/0956-7151(94)90011-6).
6. J.-B. le Graverend, J. Cormier, F. Gallerneau, S. Kruch, J. Mendez: *Mater. Des.*, 2014, vol. 56, pp. 990–97, <https://doi.org/10.1016/j.matdes.2013.12.025>.
7. J.-B. de Graverend, L. Dirand, A. Jacques, J. Cormier, O. Ferry, T. Schenk, F. Gallerneau, S. Kruch, and J. Mendez: *Metall. Mater. Trans. A*, 2012, vol. 43, pp. 3946–51, <https://doi.org/10.1007/s11661-012-1343-x>.
8. J. P. Rowe, J. W. Freeman: Report No. 4083, NACA, Washington, 1957, <https://digital.library.unt.edu/ark:/67531/metadc57105/m1/1/>. Accessed 18 May 2021.
9. J.-B. Graverend, J. Cormier, F. Gallerneau, and P. Pailmier: *Adv. Mater. Res.*, 2011, vol. 278, pp. 31–36.
10. J. Cormier, X. Milhet, and J. Mendez: *J. Mater. Sci.*, 2007, vol. 42, pp. 7780–86, <https://doi.org/10.1007/s10853-007-1645-3>.
11. R. Giraud, Z. Hervier, J. Cormier, G. Saint-Martin, F. Harmon, X. Milhet, and J. Menez: *Metall. Mat. Trans. A*, 2013, vol. A44, pp. 131–46, <https://doi.org/10.1007/s11661-012-1397-9>.
12. K.C. Chen, T.C. Chen, R.K. Shiue, and L.W. Tsay: *Metals*, 2018, vol. 8, p. 387, <https://doi.org/10.3390/met8060387>.
13. Ł. Rakoczy, M. Grudzień, L. Tuz, K. Pańcikiewicz, and A. Zielińska-Lipiec: *Adv. Mater. Sci.*, 2017, vol. 17, pp. 55–63, <https://doi.org/10.1515/adms-2017-0011>.
14. F. Hanning and J. Andersson: *Weld. World*, 2018, vol. 62, pp. 39–45, <https://doi.org/10.1007/s40194-017-0508-z>.
15. C. Kästner, M. Neugebauer, K. Schricker, and J.P. Bergmann: *J. Manuf. Mater. Process.*, 2020, vol. 4, p. 84, <https://doi.org/10.3390/jmmp4030084>.
16. F. Hanning, J. Andersson: Proceedings of the 9th International Symposium on Superalloy 718 & Derivatives: Energy, Aerospace, and Industrial Applications, 2018, pp. 917–28, https://doi.org/10.1007/978-3-319-89480-5_61.
17. A. Mashhuriazar, H. Omidvar, Z. Sajuri, C.H. Gur, and A.H. Baghdadi: *Metals*, 2020, vol. 10, p. 1453, <https://doi.org/10.3390/met1011453>.
18. Ł. Rakoczy, M. Grudzień, A. Zielińska-Lipiec: *Arch. Met. Mater.*, 2018, vol. 63, pp. 181–89, <https://doi.org/10.24425/118926>.
19. G. Zhang, C. Xiao, and M. Taheri: *J. Manuf. Process.*, 2020, vol. 52, pp. 66–78, <https://doi.org/10.1016/j.jmapro.2020.01.049>.
20. S.A. David, J.M. Vitek, S.S. Babu, L.A. Boatner, and R. Reed: *Sci. Tech. Weld. Jt.*, 1997, vol. 2, pp. 79–88, <https://doi.org/10.1179/stw.1997.2.2.79>.
21. Y.L. Hu, K. Song, X.Y. Jiang, H.O. Yang, and W.D. Huang: *Opt. Laser Tech.*, 2016, vol. 86, pp. 1–7, <https://doi.org/10.1016/j.optlastec.2016.06.008>.
22. A. Seidel, T. Finaske, A. Straubel, H. Wendrock, T. Maiwald, M. Riede, E. Lopez, F. Brueckner, and C. Leyens: *Metall. Mater. Trans. A*, 2018, vol. 49, pp. 3812–30, <https://doi.org/10.1007/s11661-018-4777-y>.
23. Y. Danis, C. Arvieu, E. Lacoste, T. Larrouy, and J.-M. Quenisset: *Mater. Des.*, 2010, vol. 31, pp. 402–16, <https://doi.org/10.1016/j.matdes.2009.05.041>.
24. G. Bidron, A. Doghri, T. Malot, F. Fournier-dit-Chabert, M. Thomas, and P. Peyre: *J. Mater. Proc. Tech.*, 2020, vol. 277, p. 116461, <https://doi.org/10.1016/j.jmatprotec.2019.116461>.
25. Ł. Rakoczy, O. Milkovič, B. Rutkowski, R. Cygan, M. Grudzień-Rakoczy, F. Kromka, and A. Zielińska-Lipiec: *Materials*, 2020, vol. 13, p. 2397, <https://doi.org/10.3390/ma13102397>.
26. Ł. Rakoczy, G. Cempura, A. Kruk, A. Czyrska-Filemonowicz, and A. Zielińska-Lipiec: *Int. J. Mater. Res.*, 2019, vol. 110, pp. 66–69, <https://doi.org/10.3139/146.111729>.
27. Ł. Rakoczy, B. Rutkowski, M. Grudzień-Rakoczy, R. Cygan, W. Ratuszek, and A. Zielińska-Lipiec: *Materials*, 2020, vol. 13, p. 4452, <https://doi.org/10.3390/ma13194452>.
28. G. Lvov, V.I. Levit, and M.J. Kaufman: *Metall Mater Trans. A*, 2004, vol. 35, pp. 1669–79, <https://doi.org/10.1007/s11661-004-0076-x>.
29. S. Tin, T.M. Pollock, and W.T. King: Carbon additions and grain boundary formation in high refractory nickel-base single crystal superalloys. *Proceedings of Superalloys 2000 Conference*, pp. 201–10.
30. S.L. Semiatin, D.W. Mahaffey, N.C. Levkulich, O.N. Senkov, and J.S. Tiley: *Metall. Mater. Trans. A*, 2018, vol. 49, pp. 6265–76, <https://doi.org/10.1007/s11661-018-4896-5>.
31. J.B. Nelson and D.P. Riley: *Proc. Phys. Soc.*, 1945, vol. 57, pp. 160–77, <https://doi.org/10.1088/0959-5309/57/3/302>.
32. E. Clementi, D.L. Raimondi, and W.P. Reinhardt: *J. Chem. Phys.*, 1967, vol. 47, pp. 1300–07, <https://doi.org/10.1063/1.1712084>.
33. F. Bertaut, P. Blum: Etude des borures de chrome. C.R. hebdomadaire des Seances Acad. Sci. 1953, vol. 236, pp. 1055.
34. J. Tiley, R. Srinivasan, R. Banerjee, G.B. Viswanathan, B. Toby, and H.L. Fraser: *Mat. Sci. Tech.*, 2009, vol. 25, pp. 1369–74, <https://doi.org/10.1179/174328409X399010>.
35. T. Grosdidier, A. Hazotte, and A. Simon: *Mat. Sci. Eng. A*, 1998, vol. 256, pp. 183–96, [https://doi.org/10.1016/S0921-5093\(98\)00795-3](https://doi.org/10.1016/S0921-5093(98)00795-3).
36. T. Grosdidier, A. Hazotte, and A. Simon: *Scr. Metall. Mater.*, 1994, vol. 30, pp. 1257–2162, [https://doi.org/10.1016/0956-716X\(94\)90255-0](https://doi.org/10.1016/0956-716X(94)90255-0).
37. M.V. Nathal: *Metall. Mater. Trans. A*, 1987, vol. 18A, pp. 1961–70, <https://doi.org/10.1007/BF02647026>.
38. M. Doi, T. Miyazaki, and T. Wakatsuki: *Mater. Sci. Eng.*, 1984, vol. 67, pp. 247–53, [https://doi.org/10.1016/0025-5416\(84\)90056-9](https://doi.org/10.1016/0025-5416(84)90056-9).
39. A.J. Ardell: *Interface Sci.*, 1995, vol. 3, pp. 119–25, <https://doi.org/10.1007/BF00207013>.
40. A. Hazotte, S. Denis: 4th Int. Conf. on residual stresses (ICRS4), Society for Experimental Mechanics, 1994, pp. 825–33.
41. A.K. Singh, N. Louat, and K. Sadananda: *Metall. Mater. Trans. A*, 1988, vol. 19A, pp. 2965–73, <https://doi.org/10.1007/BF02647723>.
42. M.A. Ali, J.V. Görler, and I. Steinbach: *Comput. Mater. Sci.*, 2020, vol. 171, p. 109279, <https://doi.org/10.1016/j.commatsci.2019.109279>.
43. N.R. Jaladurgam, H. Li, J. Kelleher, C. Persson, A. Steuwer, and M.H. Colliander: *Act. Mater.*, 2020, vol. 183, pp. 182–95, <https://doi.org/10.1016/j.actamat.2019.11.003>.
44. M. Doi: *Prog. Mater. Sci.*, 1996, vol. 40, pp. 79–180, [https://doi.org/10.1016/0079-6425\(96\)00001-1](https://doi.org/10.1016/0079-6425(96)00001-1).

45. T. Miyazaki, H. Imamura, H. Mori, and T. Kozaki: *J. Mater. Sci.*, 1981, vol. 16, pp. 1197–1203, <https://doi.org/10.1007/BF01033832>.
46. M. Doi and T. Miyazaki: *Mater. Sci. Eng.*, 1986, vol. 78, pp. 87–94, [https://doi.org/10.1016/0025-5416\(86\)90082-0](https://doi.org/10.1016/0025-5416(86)90082-0).
47. B. Bhadak, R. Sankarasubramanian, and A. Choudhury: *Metall. Mater. Trans. A*, 2018, vol. 49A, pp. 5705–26, <https://doi.org/10.1007/s11661-018-4835-5>.
48. T. Wang, X. Wang, Z. Zhao, and Z. Zhang: *Mater. High Temp.*, 2016, vol. 33, pp. 51–57, <https://doi.org/10.1179/1878641315Y.0000000006>.
49. F. Vogel, N. Wanderka, S. Matsumura, and J. Banhart: *Intermetalurgy*, 2012, vol. 22, pp. 226–30, <https://doi.org/10.1016/j.intermet.2011.11.011>.
50. R. Watanabe and T. Kuno: *Trans. Iron. Steel. Ins.*, 1976, vol. 16, pp. 437–46, <https://doi.org/10.2355/isijinternational1966.16.437>.
51. A. Hazotte, T. Grosdidier, and S. Denis: *Scr. Mat.*, 1996, vol. 34, pp. 601–08, [https://doi.org/10.1016/1359-6462\(95\)00554-4](https://doi.org/10.1016/1359-6462(95)00554-4).
52. T. Miyazaki, K. Nakamura, and H. Mori: *J. Mater. Sci.*, 1979, vol. 14, pp. 1827–37, <https://doi.org/10.1007/BF00551021>.
53. X. He, J. Zhang, Y. Peng, J. Li, J. Ding, C. Liu, X. Xia, X. Chen, and Y. Liu: *Acta. Metal. Sin.*, 2020, vol. 33, pp. 1709–26, <https://doi.org/10.1007/s40195-020-01105-0>.
54. A.J. Goodfellow, E.I. Galindo-Nava, K.A. Christofidou, N.G. Jones, T. Martin, P.A.J. Bagot, C.D. Boyer, C. Hardy, and H.J. Stone: *Metall. Mat. Trans. A*, 2018, vol. 49, pp. 718–28, <https://doi.org/10.1007/s11661-017-4336-y>.
55. Y. Chen, R. Prasathbabu, T.J. Slater, M. Bai, B. Mitchell, O. Ciuca, M. Preuss, and S.J. Haigh: *Acta Mater.*, 2016, vol. 110, pp. 295–305, <https://doi.org/10.1016/j.actamat.2016.02.067>.
56. F. Vogel, N. Wanderka, Z. Balogh, M. Ibrahim, P. Stender, G. Schmitz, and J. Banhart: *Nat. Commun.*, 2013, vol. 4, p. 2955, <https://doi.org/10.1038/ncomms3955>.
57. X. Li, K. Thornton, Q. Nie, P.W. Voorhees, and J.S. Lowengrub: *Acta Mater.*, 2004, vol. 52, pp. 5829–43, <https://doi.org/10.1016/j.actamat.2004.08.041>.
58. W.H. Tian, T. Sano, and M. Nemonoto: *Scr. Metall.*, 1986, vol. 20, pp. 933–36, [https://doi.org/10.1016/0036-9748\(86\)90469-2](https://doi.org/10.1016/0036-9748(86)90469-2).
59. H.J. Penkala, J. Wosik, and A. Czyrska-Filemonowicz: *Mat. Chem. Phys.*, 2003, vol. 81, pp. 417–23, [https://doi.org/10.1016/S0254-0584\(03\)00037-3](https://doi.org/10.1016/S0254-0584(03)00037-3).
60. M.S.A. Karunaratne, P. Carter, and R. Reed: *Acta Mater.*, 2001, vol. 49, pp. 861–75, [https://doi.org/10.1016/S1359-6454\(00\)00390-6](https://doi.org/10.1016/S1359-6454(00)00390-6).
61. J. Cernak and V. Rothova: *Acta Mater.*, 2003, vol. 51, pp. 4411–21, [https://doi.org/10.1016/S1359-6454\(03\)00276-3](https://doi.org/10.1016/S1359-6454(03)00276-3).
62. A.J. Ardell: *Scri. Mater.*, 2012, vol. 66, pp. 423–26, <https://doi.org/10.1016/j.scriptamat.2011.11.043>.
63. C.E. Campbell, W.J. Boettinger, and U.R. Kattner: *Act. Mater.*, 2002, vol. 50, pp. 775–92, [https://doi.org/10.1016/S1359-6454\(01\)00383-4](https://doi.org/10.1016/S1359-6454(01)00383-4).

Publisher's Note Springer Nature remains neutral with regard to jurisdictional claims in published maps and institutional affiliations.